CrystEngComm

PAPER

View Article Online
View Journal | View Issue

Cite this: *CrystEngComm*, 2015, **17**, 9431

$La(OH)_3:Eu^{3+}$ and $La_2O_3:Eu^{3+}$ nanorod bundles: growth mechanism and luminescence properties†

Sk. Khaja Hussain,‡ Goli Nagaraju, E. Pavitra, G. Seeta Rama Raju‡ and Jae Su Yu*

Received 21st August 2015,
Accepted 2nd November 2015

DOI: 10.1039/c5ce01688f

www.rsc.org/crystengcomm

Oriented attachment assisted self-assembled three-dimensional (3D) flower-like $La(OH)_3:Eu^{3+}$ nanorod bundles were successfully synthesized by a facile wet-chemical method. Hexamethylenetetramine played an important role in the formation of the hexagonal phase of $La(OH)_3:Eu^{3+}$ with respect to the reaction time and its concentration. No other surfactants or capping agents were used. The calcination temperature did not show any influence on the morphological texture, and the $La_2O_3:Eu^{3+}$ phase was obtained by a subsequent annealing process. The phase formation and morphological properties were confirmed by X-ray diffraction, scanning electron microscopy, and transmission electron microscopy. The photoluminescence properties were studied for both the synthesized $La(OH)_3:Eu^{3+}$ and $La_2O_3:Eu^{3+}$ samples, and also compared with that of the solid-state reaction based $La_2O_3:Eu^{3+}$ phosphor. The 3D flower-like $La_2O_3:Eu^{3+}$ nanorod bundles showed an intense red emission due to the hypersensitive $^5D_0 \rightarrow {}^7F_2$ transition with good asymmetric ratio and chromaticity coordinates. Likewise, a systematic study of the cathodoluminescence (CL) properties was carried out in detail. Furthermore, to estimate the CL potentiality, the $La_2O_3:Eu^{3+}$ phosphor was compared with a commercially available $Y_2O_3:Eu^{3+}$ red phosphor.

Introduction

Generally, the chemical and physical properties of inorganic nanostructures depend on their chemical composition, size, phase, surface chemistry, and shape.[1–5] In recent times, hierarchical three-dimensional (3D) complex architectures formed *via* self-assembly of 1D or 2D inorganic nanostructures have attracted much attention owing to their fascinating properties and versatile applications in solid-state lighting based optoelectronic applications with desired functions.[1–4] However, investigation of reasonable synthetic procedures for the construction of complex 3D architectures by facile and useful growth methods without any external assistance *via* a chemical self-assembly route is still an intensive and hot research topic.[5,6] Besides, copolymers or surfactants always play an important role in the formation procedure of novel 3D architectures due to their direct functioning during the nanostructure aggregation process along with their stabilizing quality in equilibrium systems.[5]

Moreover, trivalent rare-earth (RE^{3+}) ions such as Eu^{3+}, Tb^{3+}, Ce^{3+}, Dy^{3+}, Er^{3+}, and Tm^{3+} which activate micro-/nano-structured metal oxide host lattices have been proved to be excellent for various applications such as field-emission display (FED) devices, optoelectronic devices, biological fluorescence labelling, lasers or waveguides, *etc.*[7,8] FEDs are considered to be one of the most promising next-generation flat-panel display technologies due to their advantages of thin panel, wide viewing angle, self-emission, fast response time, high brightness/contrast, light weight, and low power consumption.[9,10] Owing to the excellent light output and color rendering properties, FEDs are of great importance in nano fields with their wonderful stability under electron bombardment.[11]

For the above-mentioned applications, RE^{3+} ions activated yttrium (Y) based host lattice materials are widely used because of their suitable crystal structure and higher chemical stability.[9,12] As compared with Y, lanthanum (La) is more abundant in RE mineral sources and lanthanum oxide (La_2O_3) is cheaper than yttrium oxide (Y_2O_3), but La based materials are still inadequate in the RE industry.[9] In general, inorganic compounds containing La^{3+} ions are identified as excellent host materials for RE activators because the RE doping levels can be controlled over a wide range without changing the host lattice crystal structure. Thus, it is essential to study La based materials practically.

In this work, we synthesized novel self-assembled $La_2O_3:Eu^{3+}$ flower-like architectures by a facile wet-chemical route. Here, hexamethylenetetramine (HMTA) is used as a surfactant. The obtained 3D flower-like morphology of the $La(OH)_3$:

Department of Electronics and Radio Engineering, Institute for Wearable Convergence Electronics, Kyung Hee University, 1 Seocheon-dong, Giheung-gu, Yongin-si, Gyeonggi-do 446-701, Republic of Korea. E-mail: jsyu@khu.ac.kr; Fax: +82 206 2820; Tel: +82 31 201 3820

† Electronic supplementary information (ESI) available. See DOI: 10.1039/c5ce01688f

‡ These authors contributed equally to this work.

Eu^{3+} precursor sample remains the same even after annealing at elevated temperatures. The formation mechanism of the self-assembled 3D flower-like lanthanum hydroxide architectures was examined as a function of reaction time and molar ratio of HMTA. The photoluminescence (PL) and cathodoluminescence (CL) properties of $La(OH)_3:Eu^{3+}$ and $La_2O_3:Eu^{3+}$ flower-like architectures were also studied.

Experimental

$La_{2(1-x)}O_3:2xEu^{3+}$ 3D flower-like nanorod bundles were synthesized by a silicon oil bath based facile wet-chemical method. The silicon oil bath was employed for temperature stability. In this synthesis, high-purity grade (Sigma-Aldrich Corp.) chemicals of lanthanum nitrate hexahydrate ($La(NO_3)_3{\cdot}6H_2O$), HMTA, and europium nitrate pentahydrate ($Eu(NO_3)_3{\cdot}5H_2O$) were used without any further purification. To prepare the $La_2O_3:Eu^{3+}$ phosphors, the composition of $La(NO_3)_3$ and $Eu(NO_3)_3{\cdot}5H_2O$ with HMTA was taken as equimolar ratio (1 : 1). $2(1-x)$ mol of $La(NO_3)_3$ and $2x$ mol of $Eu(NO_3)_3{\cdot}5H_2O$ were added to 150 mL of de-ionized (DI) water under stirring at 500 rpm. After 30 min of stirring, the equal molar ratio of HMTA was added and the stirring was continued at room temperature for 1 h to achieve complete homogenization of all the reactants. The reaction mixture beaker was then wrapped with a polyethylene cover and kept in the silicon oil bath at 75 °C for different reaction times. After the reaction progressed at a given time, the silicon oil bath temperature was gradually decreased to room temperature and then the beaker was separated from the oil bath. The obtained precipitate was centrifuged at 3000 rpm for 5 min and washed with DI water and ethanol several times. The precipitate was dried at 120 °C for a day in an ambient atmosphere. The above experimental process was performed for the formation of $La(OH)_3:Eu^{3+}$ by varying the reaction time (1, 3, 5, 7, and 10 h), and all other parameters were unchanged. Finally, self-assembled 3D flower-like nanorod bundles of Eu^{3+} ions doped $La(OH)_3$ were obtained. In order to examine the effect of HMTA, the experiment was repeated (reaction time of 10 h) under similar conditions except by varying the concentration of HMTA. Finally, the optimized precursor samples were calcined at different temperatures for further characterizations.

Characterization

The X-ray diffraction (XRD) patterns of the 3D flower-like nanorod bundles of $La(OH)_3:Eu^{3+}$ for different reaction times were recorded using a Mac Science (M18XHF-SRA) X-ray diffractometer with Cu Kα = 1.5406 Å. The morphologies of the 3D flower-like nanorod bundles were examined by using a field-emission scanning electron microscope (FE-SEM: JEOL JSM-6700) and a field-emission transmission electron microscope (FE-TEM: JEOL JEM-2100 F). The Fourier transform infrared (FTIR) spectra of the $La(OH)_3:Eu^{3+}$ and $La_2O_3:Eu^{3+}$ samples were measured by using a Thermo Nicolet – 5700 FTIR spectrophotometer with the KBr pellet technique. Thermogravimetric and differential thermal analysis (TG-DTA) data were recorded by using an SDT Q600 V8.3 Build 101 instrument with a heating rate of 5 °C min^{-1} in a nitrogen flow of 100 mL min^{-1}. The room-temperature PL and PL excitation (PLE) spectra were measured by using a Photon Technology International (PTI, USA) fluorometer. The CL properties were measured by a Gatan (UK) MonoCL3 system attached with the SEM (Hitachi S-4300 SE).

Results and discussion

Structure and morphological studies of $La(OH)_3:Eu^{3+}$

Fig. 1 shows the FE-SEM images of the self-assembled 3D flower-like morphology of $La(OH)_3:0.05Eu^{3+}$ (0.05 mol Eu^{3+} ion doped $La(OH)_3$) nanorod bundles as a function of reaction time. The following mechanism was suggested for the formation of the self-assembled 3D flower-like $La(OH)_3:0.05Eu^{3+}$ nanorod bundles. Fig. 1(a) shows the SEM images of the $La(OH)_3:0.05Eu^{3+}$ submicron rods, which were obtained after 1 h of reaction time. The average length and diameter of the submicron rods were 4.9 μm and 454 nm, respectively. For more clarity, a single submicron rod of $La(OH)_3:0.05Eu^{3+}$ is shown in the inset of Fig. 1(a). Upon extending the reaction time to 3 h, the submicron rods split into nanorod bundles (Fig. 1(b)). With further increase of reaction time to 5 h, some of the individual nanorod bundles gathered and began to form like a group through a self-assembly process, as can be seen in Fig. 1(c). When the reaction time was increased to 7 h, the $La(OH)_3$ nanorod bundles paired up and adhered to each other, showing improvement in the self-assembly process, which can be clearly observed in Fig. 1(d). At this stage, 70% of the self-assembly process was completed and the structure appeared as a flower. Finally, when the reaction time was increased to 10 h, the self-assembly process was completed and $La(OH)_3$ nanorod bundles with 3D flower-like morphologies were observed, as shown in Fig. 1(e). For in-depth analysis of the nanorod bundle based $La(OH)_3$ flower-like morphology, the 3D image was drawn using the interactive 3D surface plot of ImageJ software, as shown in Fig. 1(f). The interactive analysis of the top and bottom views of the $La(OH)_3$ 3D flower-like structures clarifies that they were grown with the combination of almost uniform sized and crystal splitting based nanorod bundles.

The TEM image of the 3D flower-like $La(OH)_3:0.05Eu^{3+}$ sample (Fig. 2(a) and (b)) is well consistent with the SEM image of a similar sample. The corresponding selected area electron diffraction (SAED) pattern for the edge of the single nanorod bundle of $La(OH)_3:Eu^{3+}$ is shown in Fig. 2(c). The SAED pattern covers a number of bright spots in an irregular manner, revealing the nanocrystalline nature, and the diffraction spots were indexed to the pure hexagonal phase of $La(OH)_3$ with the space group $P6_3/m$ (176), corresponding to the (201) and (211) reflections. The high-resolution TEM (HRTEM) image of the precursor sample shows the imaging characteristics of the hexagonal structure. Here, the

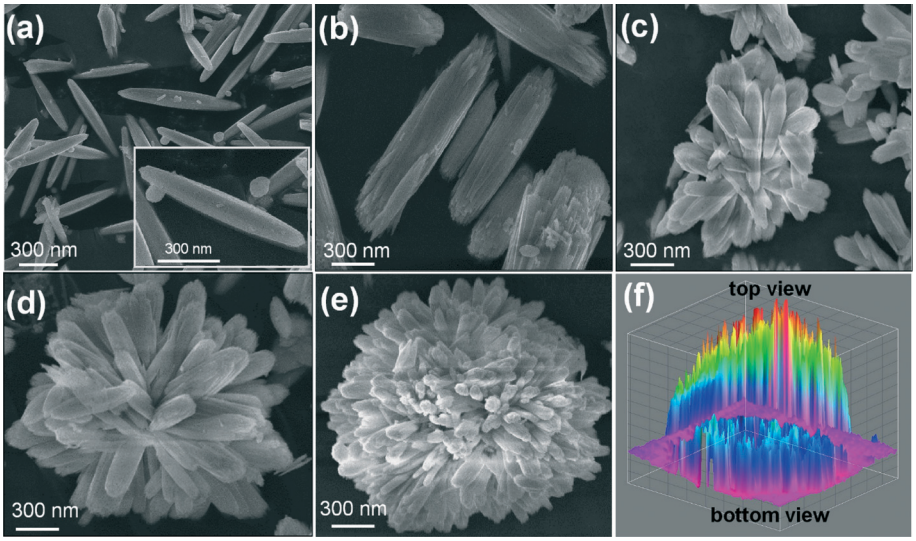

Fig. 1 FE-SEM images of the as-prepared $La(OH)_3$:0.05Eu^{3+} samples at different reaction times: (a) 1 h, (b) 3 h, (c) 5 h (d) 7 h, and (e) 10 h. (f) 3D graphical top and bottom views of the self-assembled $La(OH)_3$ nanorod bundles.

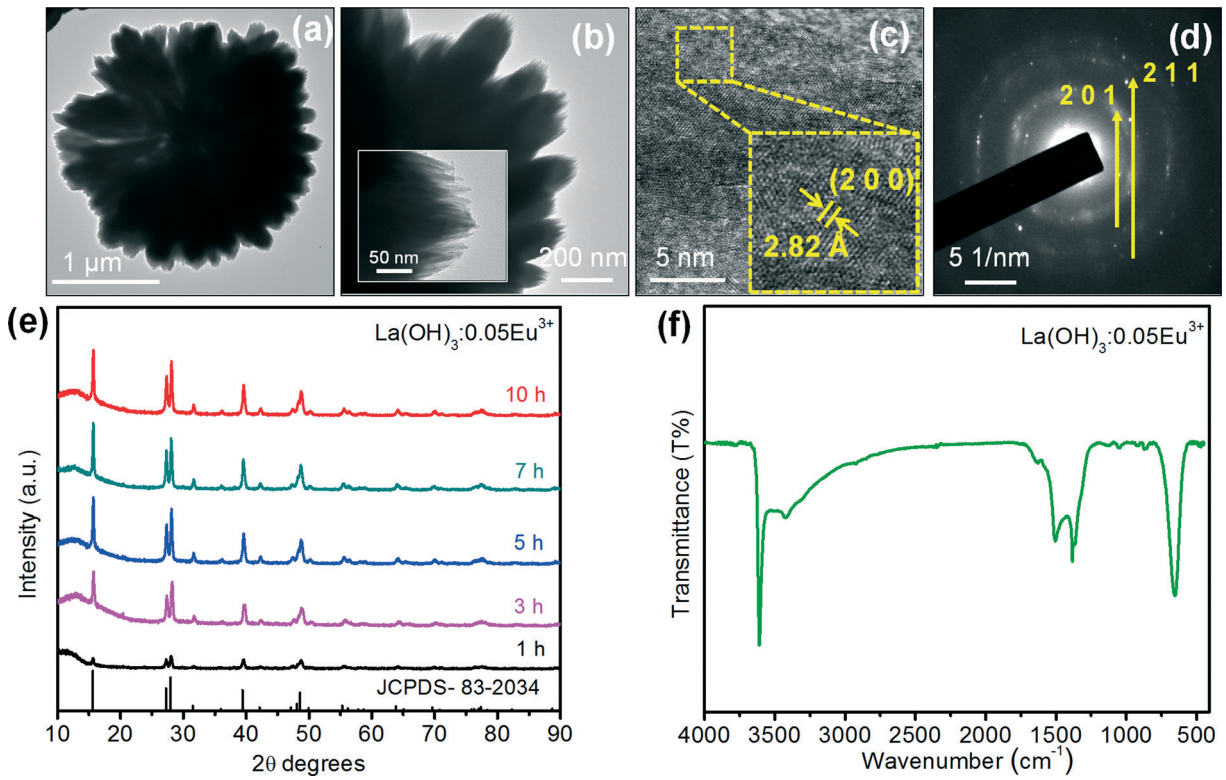

Fig. 2 (a) TEM image, (b) high-magnification TEM image, (c) HRTEM image, and (d) SAED pattern of the as-prepared 3D flower-like $La(OH)_3$:0.05Eu^{3+} nanorod bundles. (e) XRD patterns of the as-prepared $La(OH)_3$:0.05Eu^{3+} samples at different reaction times. (f) FTIR spectra of the optimized $La(OH)_3$:0.05Eu^{3+} sample at the reaction time of 10 h.

d-spacing of 2.82 Å corresponds to the distance of the (200) plane.

XRD analysis of $La(OH)_3$:0.05Eu^{3+}

The phase purity of the as-prepared $La(OH)_3$:0.05Eu^{3+} samples was examined by XRD. Fig. 2(e) shows the XRD patterns of the pure $La(OH)_3$:0.05Eu^{3+} samples obtained at different reaction times of 1, 3, 5, 7 and 10 h. At 1 h of reaction time, the intensities of the diffraction peaks were very weak. However, the intensity of the diffraction peaks also increased with increasing the reaction time, indicating that the crystallinity of the $La(OH)_3$:0.05Eu^{3+} samples depends on the reaction time.

All the diffraction peaks are attributed to the hexagonal crystal phase, which are in good agreement with the standard JCPDS card [83-2034] with the space group $P6_3/m$ (176). This clearly indicates that a long reaction time is required for the growth of self-assembled 3D flower-like $La(OH)_3$:$0.05Eu^{3+}$ nanorod bundles with higher crystallinity because it increases the ionic transfer rate and separation of nuclei which allows complete crystal growth.[13] No impurity phase is affected by the Eu^{3+} ions at the current doping levels, indicating that Eu^{3+} ions are completely dissolved into the La^{3+} sites of the $La(OH)_3$ host lattice. It is well known that the pure phase is favorable for the luminescence properties of phosphors. Moreover, the full width at half maximum (FWHM) values of the strongest diffraction peaks were used to calculate the crystallite size from the well-known Scherer equation of $D_{hkl} = k\lambda/\beta\cos\theta$,[14] where D is the average grain size, k (0.9) is the shape factor, λ is the X-ray wavelength (1.5406 Å), β is the FWHM and θ is the diffraction angle of the observed peak. The calculated average crystallite sizes at 1, 3, 5, 7 and 10 h were 26.6, 40, 42.4, 49.3, and 55.7 nm, respectively.

FTIR study of $La(OH)_3$:$0.05Eu^{3+}$

FTIR is also one of the additional characterization techniques used to examine the presence of hydroxyl (OH^-) groups and the formation of $La(OH)_3$. Fig. 2(f) shows the FTIR spectrum of the 3D flower-like $La(OH)_3$:$0.05Eu^{3+}$ nanorod bundles synthesized at 10 h of reaction time. The spectrum showed an intense and sharp band at 3613 cm^{-1}, corresponding to the stretching and bending O–H vibrations of $La(OH)_3$.[15,16] The bands at 3424 and 1635 cm^{-1} correspond to the O–H vibration from the absorbed water on the sample surface.[13,15,16] The sharp peak at 1390 cm^{-1} is attributed to the bending mode of O–H.[13,16] The band at nearly 660 cm^{-1} is related to the bending vibration of La–O–H.[15] This FTIR analysis of the as-prepared $La(OH)_3$ sample indeed indicates the presence of OH^- groups.

Growth mechanism of $La(OH)_3$:Eu^{3+} 3D architectures

In order to explore the growth mechanism of the 3D flower-like $La(OH)_3$:Eu^{3+} nanorod bundle morphology, various experiments were performed based on the reaction time and HMTA concentration. Herein, HMTA was used as an additive. In the initial stage of the growth process, HMTA hydrolyzed slowly in DI water upon heating and gradually released the OH^- ions due to its weak basic nature. The following chemical reaction may occur in the growth process:[13,17]

$$(CH_2)_6N_4 + 6H_2O \rightarrow 6HCHO + 4NH_3$$

$$4NH_3 + H_2O \rightarrow 4NH_4^+ + OH^-$$

The generated OH^- ions combine with La^{3+} ions in the growth solution and are precipitated as a $La(OH)_3$ colloid as follows:[13,17]

$$La^{3+} + 3OH^- \rightarrow La(OH)_3$$

In this mechanism, HMTA played a key role in forming the self-assembled 3D flower-like morphologies of $La(OH)_3$:$0.05Eu^{3+}$ nanorod bundles with respect to the reaction time. No other templates/surfactants/emulsions were used in this experiment. It has been reported that when HMTA is used as a capping agent, it produces more OH^- ions in the solution at a certain reaction temperature.[17,18] A possible growth mechanism involved in the process of the formation of self-assembled 3D flower-like nanorod bundles is illustrated schematically in Fig. 3. In this synthesis, at the initial stage, individual submicron rods of $La(OH)_3$:$0.05Eu^{3+}$ are formed with the pure hexagonal phase as explained in the XRD section, indicating the occurrence of fast nucleation. The fast nucleation is caused by the presence of excess NH_4^+ ions in the reaction media, which accelerates the reaction between La^{3+} and OH^- ions. With further increase of reaction time to 3 h, the submicron rods begin to split into nanorod bundles within the same unit due to crystal splitting, and the resulting submicron rods look like nanorod bundles. The nature of crystal splitting varies depending on both kinetic and thermodynamic factors which are related to the selected material.[19–21] From the literature and the above proposed reaction mechanism, it is assumed that the excess of NH_4^+ ions strongly affects the formation of nanorod bundles.[19–21] It is observed that as the reaction time further increases to 5 h, the splitting process is saturated, and the nanorod bundles tend to coalesce with each other by an oriented attachment assisted self-assembly process. This process usually depends on the size and surface capping of nanoparticles.[18,22] It can be also noted that the presence of NH_4^+ ions not only induces the fast reaction but also acts as a soft template, thus prompting the oriented attachment assisted self-assembly process.[18,22] The self-assembly process continues as the reaction time increases to 7 h. Finally, an anisotropic natured 3D flower-like morphology is observed after completing the reaction at 10 h. From the observed results, we are able to describe the growth mechanism of $La(OH)_3$ 3D flower-like structures as involving a sequence of nucleation, crystal splitting and self-assembly process assisted by oriented attachment.

To explore the role of HMTA concentration in the growth process of the self-assembled 3D flower-like morphologies of $La(OH)_3$:Eu^{3+} nanorod bundles, a series of experiments were performed at 10 h of reaction time by varying the molar ratio of HMTA/$La(NO_3)_3$ such as (0.5 : 1) (1 : 1) and (1.5 : 1); the resulting SEM images are presented in Fig. S1 of the ESI.† At a molar ratio of 0.5HMTA and 1$La(NO_3)_3$, the synthesized $La(OH)_3$:Eu^{3+} samples did not yield the perfect 3D flower-like morphology. It is noticed that the amount of HMTA is insufficient to produce NH_4^+ ions for the completion of the crystal splitting process and stabilization of La^{3+} ions in the solution. As a result, self-assembly of submicron rods with a partial 3D flower-like morphology at a low crystal splitting rate was observed and the corresponding low- and high-magnification SEM images are presented in Fig. S1(a) and (b),† respectively. Fig. S1(c) and (d)† shows clear views of the low- and high-magnification SEM images of the self-assembled

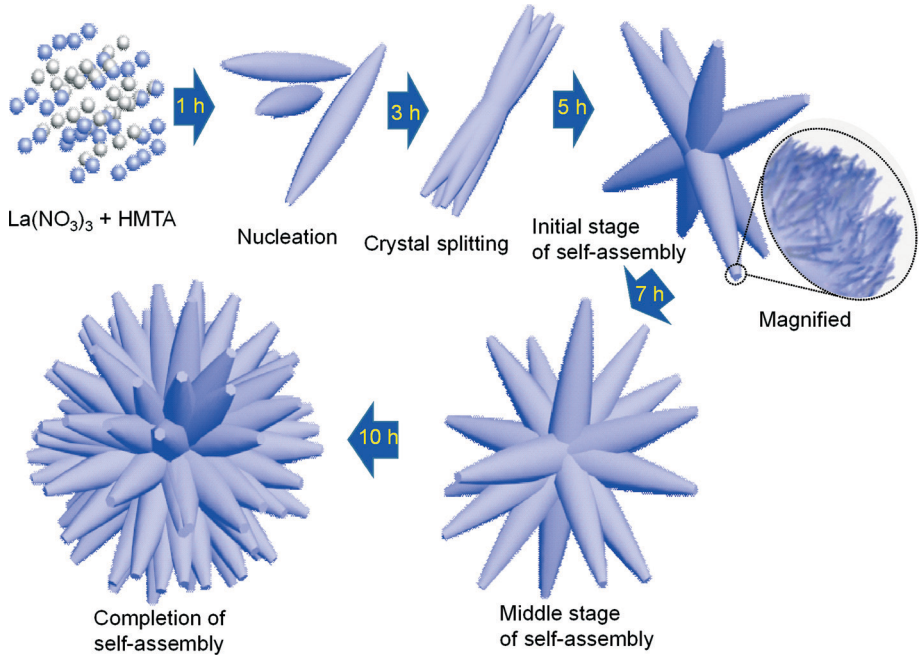

Fig. 3 Schematic for the formation process of the $La(OH)_3$:0.05Eu^{3+} sample.

perfect 3D flower-like morphologies of $La(OH)_3$:Eu^{3+} nanorod bundles at a molar ratio of 1HMTA and 1$La(NO_3)_3$. Finally, at a molar ratio of 1.5HMTA and 1$La(NO_3)_3$, aggregation of the nanorod bundles took place and a disordered self-assembly process occurred due to the oversaturation of HMTA. The low- and high-magnification SEM images of the aggregated 3D flower-like morphology of $La(OH)_3$:Eu^{3+} samples are shown in Fig. S1(e) and (f).† Therefore, from the above reasonable and scientific study, the concentration of HMTA played a crucial role in controlling the perfect 3D flower-like morphologies of $La(OH)_3$:Eu^{3+} nanorod bundles.

Effect of calcination temperature

Thermal decomposition of RE hydroxide is a simple and universal route towards tailored RE and metal oxides. Fig. 4 shows the thermal behavior and weight loss percentage (%) of the as-prepared $La(OH)_3$:0.05Eu^{3+} sample. The sample was characterized by TG/DTA analysis from room temperature to 1000 °C. TG/DTA measurements were conducted to determine the transformation of $La(OH)_3$ to LaOOH and La_2O_3.[23–26] The total weight loss of the $La(OH)_3$ sample was 19.16 wt%, and it could be seen in the TG curve. From the TG curve, it was observed that the weight loss occurred in three steps up to 800 °C. The weight loss percentage in the first step was 1.87%. This is attributed to the transformation of $La(OH)_3$ to LaOOH up to approximately 250 °C.[25,26] In the second step, the major weight loss occurred up to 12.92%, related to the dehydration of LaOOH and the formation of La_2O_3 around 600 °C.[11,24,25] Furthermore, 4.37% weight loss occurred due to the removal of intercalated nitrate ions up to 800 °C.[25] The theoretical values for weight loss of the mentioned transformation were reported to be 9.5 and 4.5%, respectively, which were in agreement with the reported data.[23,25,26] The DTA spectrum revealed two major exothermic peaks. One of the peaks occurred at 335 °C, which is related to the second and major weight loss, indicating good agreement with the transformation of $La(OH)_3$ into LaOOH as reported earlier.[25] It is well known that LaOOH is an intermediate phase with a monoclinic crystal structure and the space group is $P2_1/m$ (No. 11).[25] The second peak observed at approximately 652 °C is associated with the dehydration of LaOOH and the formation of La_2O_3.[25,26] Therefore, from the TG-DTA data, it is found that more heat is required to eliminate the hydroxyl group and form La_2O_3.

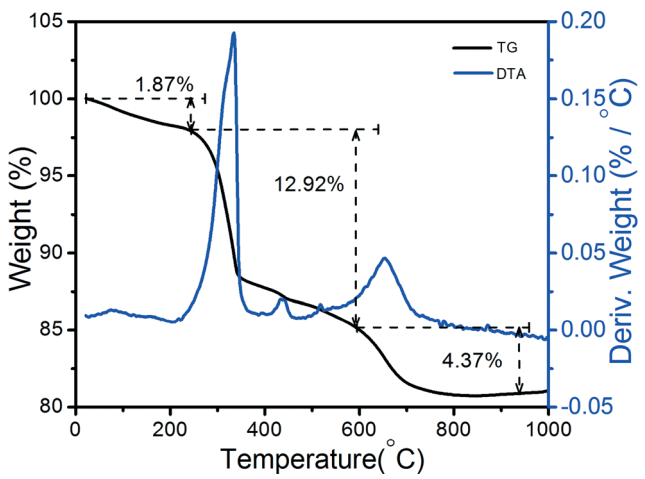

Fig. 4 TG/DTA curves of the $La(OH)_3$:0.05Eu^{3+} sample.

XRD analysis and FTIR study of La_2O_3:Eu^{3+}

To obtain the product La_2O_3:0.05Eu^{3+} from $La(OH)_3$:0.05Eu^{3+} samples, the precursor samples were calcined for 6 h at 600

and 800 °C (raising the temperature with 1 °C min^{-1}), and the suitable calcination temperature was optimized. Fig. 5(a) shows the XRD patterns of $La(OH)_3$:0.05Eu^{3+} at different calcination temperatures. From the XRD patterns, the low intensity of oxide diffraction peaks was observed at 600 °C, indicating that it requires a high temperature to be converted to La_2O_3:0.05Eu^{3+} with better crystallinity. After being calcined at 800 °C, all the diffraction peaks were readily indexed to the pure hexagonal phase of La_2O_3:0.05Eu^{3+} with the space group $P\bar{3}m1$(164), which agrees well with the standard JCPDS card [05-0602]. Fig. S2 of the ESI† shows the XRD patterns of La_2O_3:Eu^{3+} samples as a function of Eu^{3+} ion concentration. Notably, there were no impurity peaks found from any other secondary phases, indicating that $La(OH)_3$:Eu^{3+} was completely converted into La_2O_3:Eu^{3+} after calcination at 800 °C. Moreover, the functional groups of La_2O_3:0.05Eu^{3+} were further examined by FTIR spectroscopy. Fig. 5(b) shows the FTIR spectra of the La_2O_3:0.05Eu^{3+} sample with self-assembled 3D flower-like nanorod bundles. From the FTIR spectra, it is clearly noticed that there is no major intense and sharp peak at 3613 cm^{-1} related to the stretching and bending vibration of O–H.[7,16] Also, the observed remaining peaks at 3424 and 1635 cm^{-1} had weak and broad absorption bands, which shows the existence of water molecules on the surface of La_2O_3:0.05Eu^{3+} nanostructures.[13] The bands between 850 and 500 cm^{-1} indicate the La–O bending vibrational frequencies.[7,16]

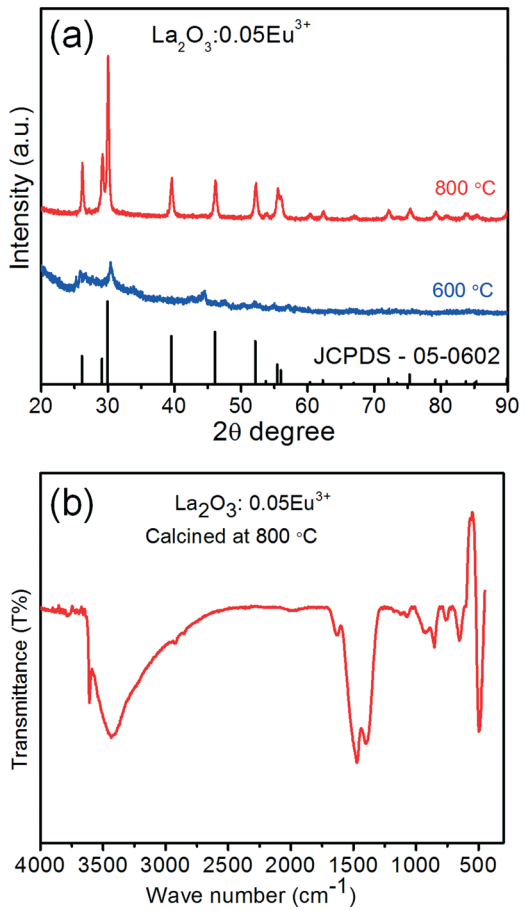

Fig. 5 (a) XRD patterns of the calcined La_2O_3:0.05Eu^{3+} samples at 600 and 800 °C. (b) FTIR spectrum of the calcined La_2O_3:0.05Eu^{3+} sample at 800 °C.

Structural and morphological studies of La_2O_3:Eu^{3+} 3D architectures after calcination process

To examine the stability of the 3D flower texture, the typical FE-SEM, TEM, and HRTEM images, and SAED patterns of La_2O_3:0.05Eu^{3+} samples after calcination at 600 and 800 °C were obtained (see Fig. 6). The SEM images in Fig. 6(a)(i) and (b)(i) revealed that the self-assembled 3D flower-like nanorod bundles inherited their original morphology. However, from a close observation of the high-magnification SEM image (Fig. 6(a)(ii)), the surface of the self-assembled 3D flower-like nanorod bundles became rough with sharp chews as compared with the $La(OH)_3$:0.05Eu^{3+} precursor. This might be due to the gradual elimination of OH and the increased particle size as a result of increased crystallinity during the calcination process (600 °C). This situation can be also confirmed by analysis of TEM images, as shown in Fig. 6(a)(iii) and (a)(iv). When the calcination temperature was further increased to 800 °C, without changing the 3D flower texture, the particles in the nanorod bundles became bigger and coalesced or merged with each other, and the sharpness of the chews completely vanished. The merging is related to the melting process because the surface-to-volume ratio of the nanoparticles is relatively high, and at high temperatures, the surface energy substantially affects the interior bulk properties of the materials. For further clarification, the high-magnification SEM and TEM images are shown in Fig. 6(b)(ii), (b)(iii) and (b)(iv). However, the conversion of $La(OH)_3$:0.05Eu^{3+} to La_2O_3:0.05Eu^{3+} did not change the morphology, and such a transformation is common for decomposition of RE metal hydroxide and metal compounds.[15,25] The original texture morphologies were maintained perhaps due to the higher activation energies needed for the collapse of these structures, and this morphology-inheriting method is a facile and general strategy for designing morphology-dependent functional compounds.[15,25] The fine structure of the as-prepared La_2O_3:0.05Eu^{3+} samples was further studied from the HRTEM images and SAED patterns. The SAED patterns of the calcined samples confirmed their nanocrystalline nature by producing a number of bright spots in an irregular manner and exhibiting the (100) (110) and (102) reflections, as shown in Fig. 6(a)(iv) and (b)(iv). The corresponding HRTEM image shows the imaging characteristics of the hexagonal La_2O_3 structure with a *d*-spacing of 3.35 Å, corresponding to the (100) plane of the sample calcined at 600 °C (Fig. 6(a)(v)). In a similar way, the sample calcined at 800 °C exhibited a *d*-spacing of 2.92 Å, corresponding to the (101) plane (Fig. 6(b)(v)). Fig. 7 shows the elemental mapping of the La_2O_3:Eu^{3+} sample, which was analyzed by energy dispersive X-ray (EDX) spectroscopy. The EDX spectrum was taken for a single self-assembled 3D flower in TEM mode and no elements other than La, O, and Eu appeared from the measurement, which supports the XRD results.

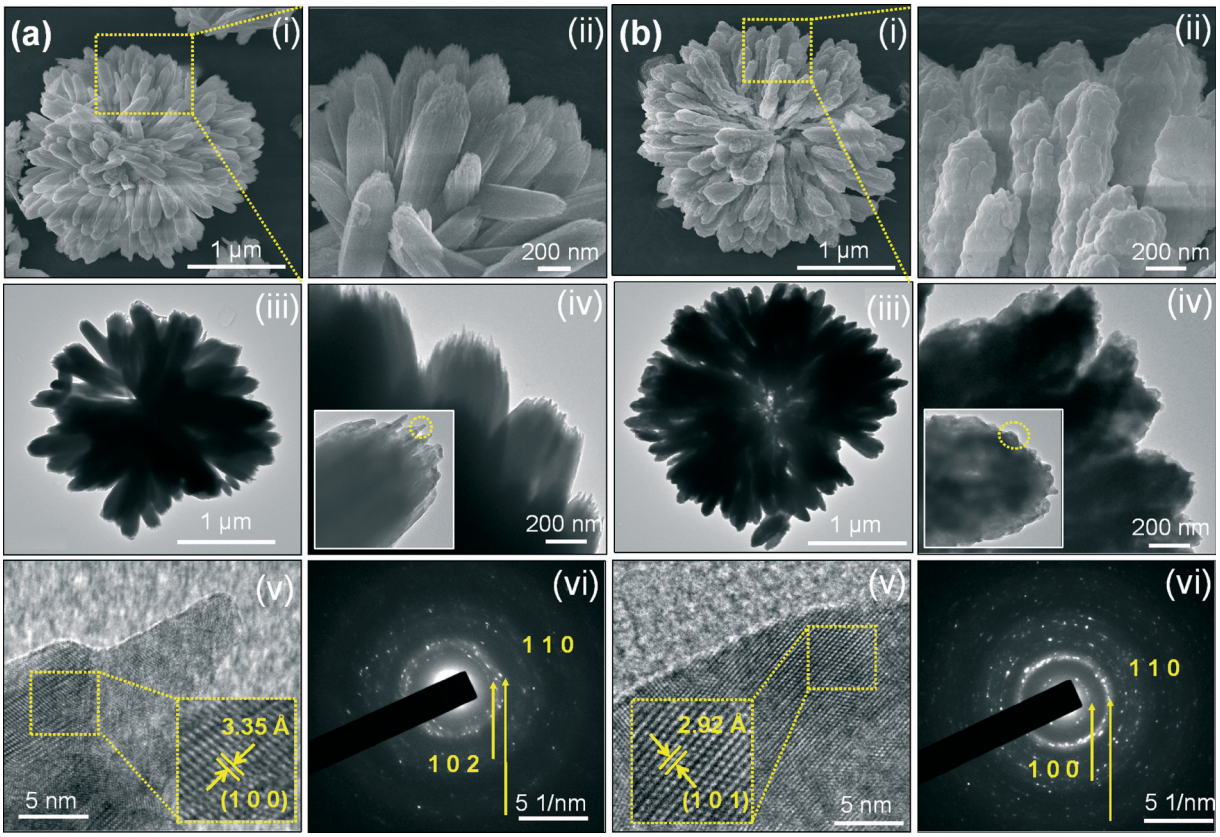

Fig. 6 (a) (i and ii) SEM and magnified SEM images of the $La_2O_3:Eu^{3+}$ single flower, (iii and iv) TEM and magnified TEM images of the $La_2O_3:Eu^{3+}$ single flower, and (v and vi) HRTEM image and SAED pattern of the $La_2O_3:Eu^{3+}$ sample after being calcined at 600 °C. (b) (i and ii) SEM and magnified SEM images of the $La_2O_3:Eu^{3+}$ single flower, (iii) TEM and magnified TEM images of the $La_2O_3:Eu^{3+}$ single flower, and (v and vi) HRTEM image and SAED pattern of the $La_2O_3:Eu^{3+}$ sample after being calcined at 800 °C.

Photoluminescence properties

Fig. 8(a) and (b) shows the PLE spectra of the $La(OH)_3:0.05Eu^{3+}$ and $La_2O_3:Eu^{3+}$ samples by monitoring the emission wavelengths at 611 and 625 nm, respectively. The dominant excitation wavelength was observed at 393 nm for the $La(OH)_3$ sample along with some weak f–f transitions. However, no charge transfer band

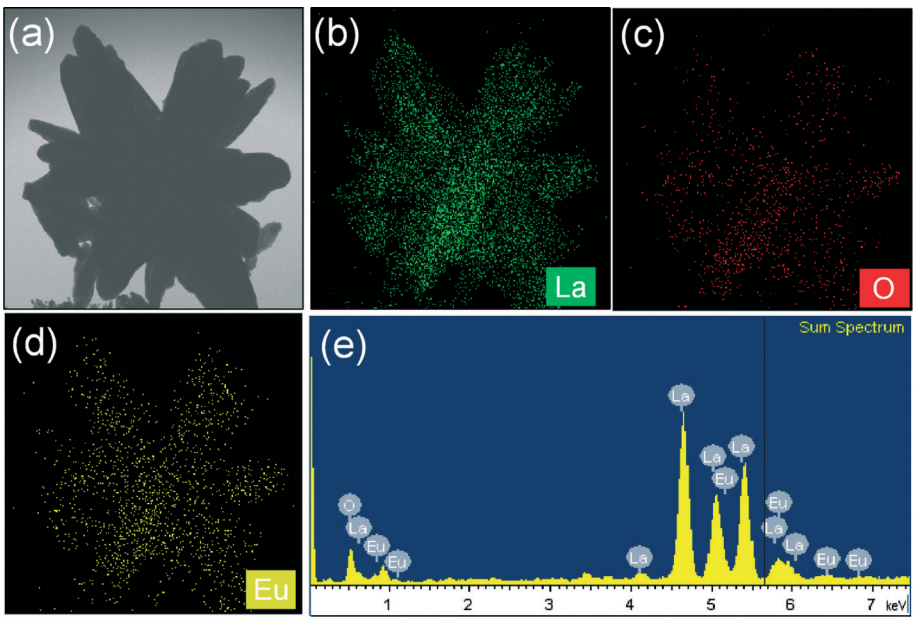

Fig. 7 (a) TEM image, (b–d) elemental mapping images, and (e) EDX spectrum for the as-prepared $La_2O_3:Eu^{3+}$ sample after being calcined at 800 °C.

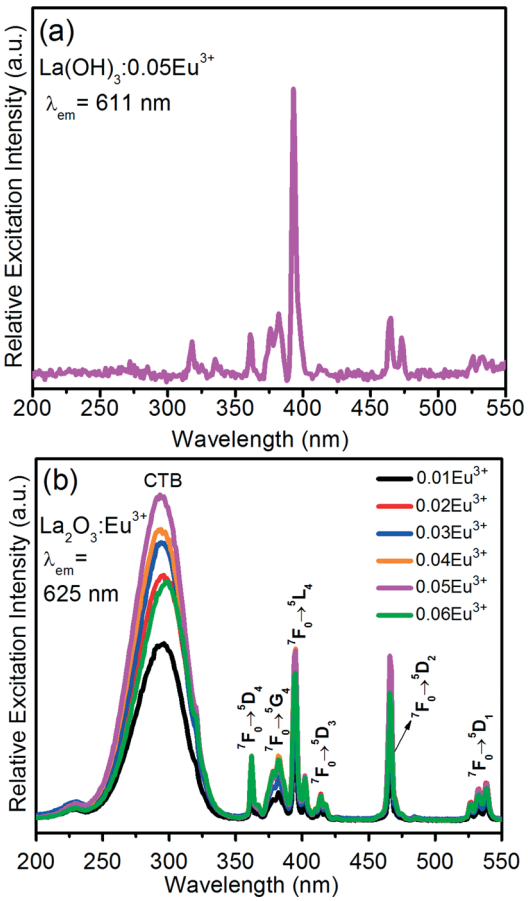

Fig. 8 PLE spectra of (a) the $La(OH)_3$:0.05Eu^{3+} sample after completing the reaction at 10 h and (b) the La_2O_3:Eu^{3+} samples as a function of Eu^{3+} ion concentration.

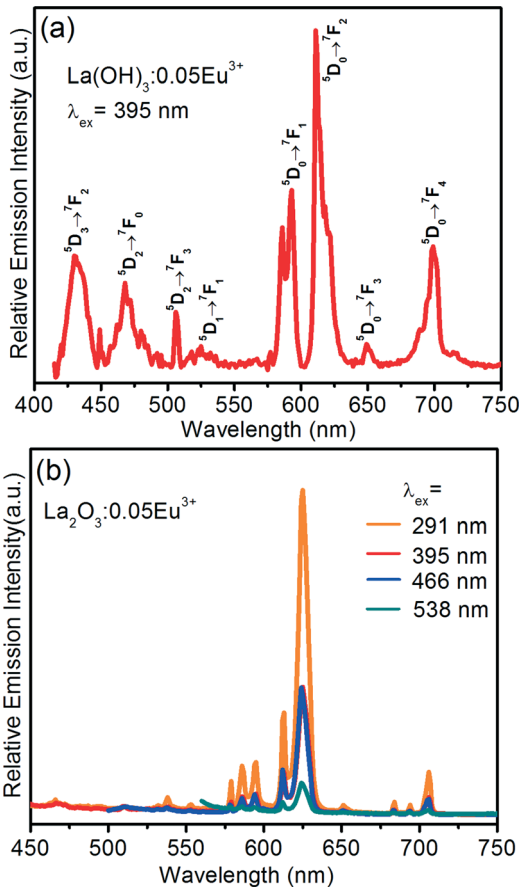

Fig. 9 PL spectra of (a) the $La(OH)_3$:0.05Eu^{3+} sample after completing the reaction at 10 h and (b) the La_2O_3:0.05Eu^{3+} sample as a function of excitation wavelength.

(CTB) was observed in the higher energy region. Fig. 8(b) also shows the PLE spectra of La_2O_3:Eu^{3+} as a function of Eu^{3+} ion concentration. The PLE spectra exhibited the CTB with band maxima at 291 nm along with the f–f transitions at 361 nm ($^7F_0 \rightarrow {}^5D_4$), 382 nm ($^7F_0 \rightarrow {}^5G_4$), 395 nm ($^7F_0 \rightarrow {}^5L_6$), 414 nm ($^7F_0 \rightarrow {}^5L_6$), 466 nm ($^7F_0 \rightarrow {}^5D_2$), and 538 nm ($^7F_0 \rightarrow {}^5D_1$).[27] It is noticed that the CTB appears for the calcined samples because the distance between the completely filled 2p orbital of O^{2-} ions and the partially filled 4f orbital of Eu^{3+} ions decreases due to the increased crystallite or particle size. But, for the $La(OH)_3$:0.05Eu^{3+} phosphor, the charge transfer between the O^{2-} and Eu^{3+} ions is almost null due to the presence of OH^- group and the smaller particle sizes. These sharp excitation peaks of Eu^{3+} indicate that violet and blue laser diodes/light-emitting diodes are also efficient pumping sources in obtaining Eu^{3+} emissions.

Fig. 9(a) shows the PL spectra of the $La(OH)_3$:0.05Eu^{3+} sample with self-assembled 3D flower-like nanorod bundles under an excitation wavelength of 395 nm. Fig. 9(b) shows the PL spectra of the La_2O_3:0.05Eu^{3+} sample as a function of excitation wavelength. The $La(OH)_3$:0.05Eu^{3+} sample revealed intense emission peaks in the blue, orange and red regions due to the emissions coming from higher energy states like $^5D_3$ (430 nm), $^5D_2$ (468 nm), $^5D_1$ (532 nm) and $^5D_0$ (592, 610, 650, and 700 nm). Among them, an intense emission band was observed due to the forced electric–dipole/hypersensitive transition at 611 nm ($^5D_0 \rightarrow {}^7F_2$). However, La_2O_3:Eu^{3+} 3D flower-like nanorod bundles show emission bands only from the $^5D_0$ metastable state. An intense emission band appeared at 625 nm due to the ($^5D_0 \rightarrow {}^7F_2$) transition of Eu^{3+} ions.[28,29] In both cases, the intense emission peaks confirmed that the Eu^{3+} ions are located at the sites without inversion symmetry. The moderate intense emission bands at 578 nm due to the ($^5D_0 \rightarrow {}^7F_0$) transition and the bands at 586 and 594 nm correspond to the magnetic dipole ($^5D_0 \rightarrow {}^7F_1$) transition that appeared in the PL spectra.[28,29] The PL spectra exhibited similar emission bands under different excitation wavelengths. The intense emission was observed under an excitation wavelength of 291 nm. Therefore, we presented the PL spectra as a function of Eu^{3+} ion concentration at 291 nm of excitation wavelength.

Fig. 10 shows the PL spectra of the La_2O_3:Eu^{3+} 3D flower-like nanorod bundle samples as a function of Eu^{3+} ion concentration. When the Eu^{3+} ion concentration increased from 1 to 5 mol%, the emission intensity also increased, and with further increase of Eu^{3+} ion concentration above 6 mol%, the emission intensity decreased due to the concentration quenching. The concentration quenching might be elucidated in the La_2O_3

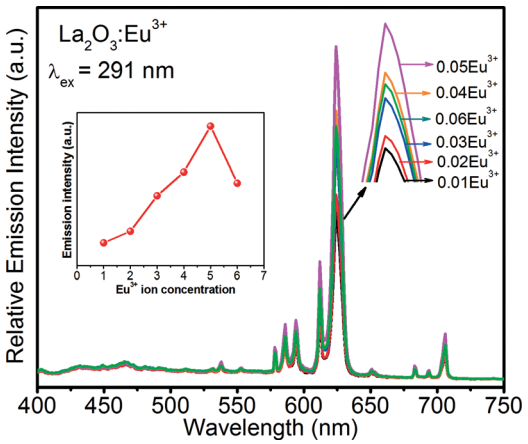

Fig. 10 PL spectra of the $La_2O_3:Eu^{3+}$ samples as a function of Eu^{3+} ion concentration.

host lattice by the following two factors: (i) when the Eu^{3+} concentration is increased, the resonance between the activator ions increases, which results in the enhancement of excitation migration, and thus the excitation energy reaches the quenching centers, and (ii) the Eu^{3+} ions are paired or coagulated in the La_2O_3 host lattice and changed into quenching centers. The above results suggest that the physical and chemical properties of the $La_2O_3:Eu^{3+}$ nanophosphors are stable at the optimum concentration of 5 mol% for Eu^{3+} ions. The correlation between the concentration of Eu^{3+} ions and emission intensity is also shown in the inset of Fig. 10.

To explore the richness of the red emission of the $La_2O_3:0.05Eu^{3+}$ phosphor with 3D flower-like nanorod bundles, the present phosphor was compared with the bulk $La_2O_3:0.05Eu^{3+}$ phosphor, which was prepared by a solid-state reaction method under the same composition and annealed at 800 °C for 5 h, as shown in Fig. 11. Under 291 nm excitation, it can be seen that both phosphors displayed similar emission behaviors except intensities. However, at similar measurement conditions, the emission intensity of the $La_2O_3:0.05Eu^{3+}$ nanorod bundle phosphor was much higher than that of the

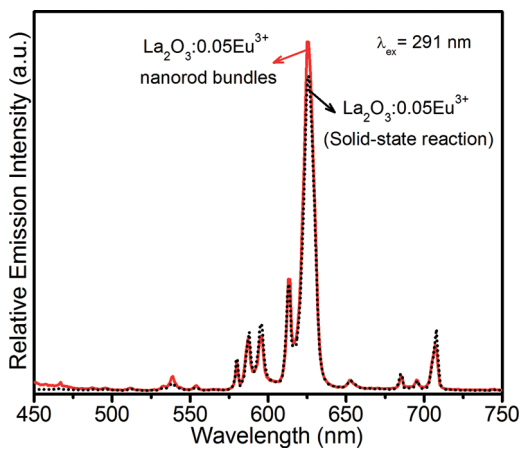

Fig. 11 PL intensity comparison of $La_2O_3:0.05Eu^{3+}$ phosphor with 3D flower-like nanorod bundles with solid-state reaction based $La_2O_3:0.05Eu^{3+}$ phosphor.

phosphor prepared by a solid-state reaction method. It is also noticed that the most intense transition for both phosphors appears at 625 nm, which is the best component for red emission. The *R*/*O* values for the $La_2O_3:0.05Eu^{3+}$ nanorod bundle phosphor and solid-state reaction based $La_2O_3:0.05Eu^{3+}$ phosphor were about 6.40 and 4.32. It is well known that a higher *R*/*O* value indicates improved color purity of the red component.[30]

Cathodoluminescence properties

In order to explore the potential of the as-prepared self-assembled 3D flower-like nanorod bundles of $La(OH)_3:0.05Eu^{3+}$ and $La_2O_3:0.05Eu^{3+}$ for use as CL materials, their CL properties were investigated in detail. Fig. 12 shows the CL spectra of the optimized (a) $La(OH)_3:0.05Eu^{3+}$ and (b) $La_2O_3:0.05Eu^{3+}$ samples under low electron beam excitation (acceleration voltage: 5 kV and filament current: 55 μA). From the CL spectra of both the samples, somewhat different behaviors were observed as compared to the PL spectra. In the PL spectra, the $La(OH)_3:0.05Eu^{3+}$ sample showed moderately intense emission bands in the blue and deep red regions, while in the CL spectra, the emission bands did not appear in the blue region, but a highly intense emission

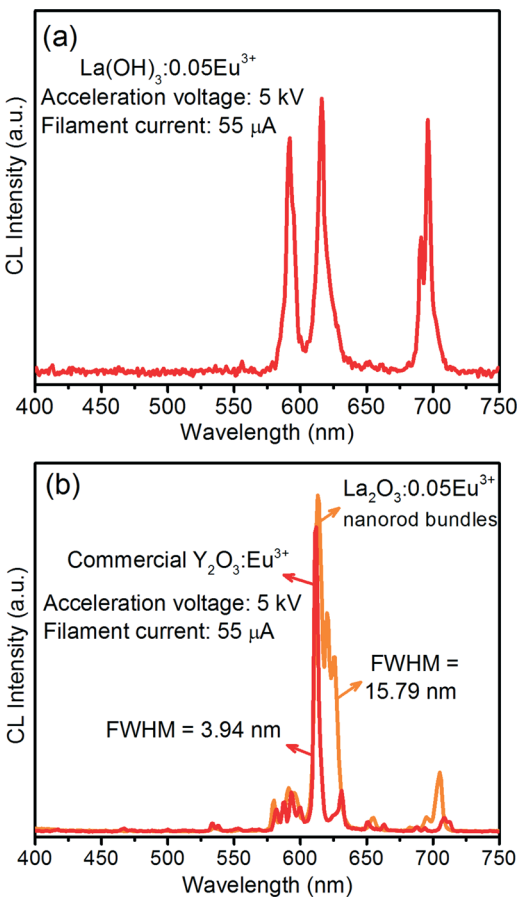

Fig. 12 (a) CL spectrum of the $La(OH)_3:0.05Eu^{3+}$ nanorod bundle phosphor. (b) Comparison of the CL spectra of the commercial $Y_2O_3:Eu^{3+}$ phosphor and $La_2O_3:0.05Eu^{3+}$ nanorod bundle phosphor at an accelerating voltage of 5 kV and a filament current of 55 μA.

band appeared in the deep red region due to the ($^5D_0 \rightarrow {}^7F_4$) transition. For both $La(OH)_3$:0.05Eu^{3+} and La_2O_3:0.05Eu^{3+} samples, a strong emission band appeared at 615 nm due to the ($^5D_0 \rightarrow {}^7F_2$) transition. The fact that the emission bands were not observed in the blue region and the intense emission was observed in the deep red region can be explained by different mechanisms in the CL process as compared to the PL process.[14] In CL, the high energy electrons excite almost all the activator ions due to the deeper penetration depth, and thus there is a possibility of cross-relaxation between Eu^{3+} ions. As a result, the energy transfer process occurs from the higher energy levels to the lower metastable states.

To estimate the possibility of the phosphor for the desired application, it is a better approach to establish their efficiency. The CL efficiency has been analyzed by the radiant efficiency (η) and the luminous efficiency, *i.e.*, brightness (L) of the given material. According to the literature,[31] to understand the CL efficiency of the red emitting La_2O_3:0.05Eu^{3+} phosphor with self-assembled 3D flower-like nanorod bundles, η and L can be compared with those of the commercially available Y_2O_3:Eu^{3+} phosphor under an accelerating voltage of 5 kV and a filament current of 55 μA, as shown in Fig. 12(b). From the comparative CL spectra, the commercial Y_2O_3:Eu^{3+} phosphor revealed quite sharp emission peaks in the red region with band maxima at 611 nm, exhibiting a FWHM value of 3.94 nm. The synthesized La_2O_3:0.05Eu^{3+} phosphor showed a broad band between 604 and 638 nm with band maxima at 615 nm and the calculated FWHM value is 15.79 nm. It is clear that the La_2O_3:0.05Eu^{3+} phosphor with 3D flower-like nanorod bundles exhibited a higher CL intensity, such as brightness, and also a 4 times higher FWHM emission value (emission peak area) than the commercial Y_2O_3:Eu^{3+} phosphor. Therefore, the La_2O_3:0.05Eu^{3+} 3D flower-like nanorod bundle phosphor might be more efficient than the commercially available Y_2O_3:Eu^{3+} phosphor.

Fig. 13 shows the CL intensities of the $La(OH)_3$:0.05Eu^{3+} and La_2O_3:0.05Eu^{3+} phosphors as a function of filament current and accelerating voltage. From Fig. 13(a) and (c), it is evident that when the accelerating voltage was fixed at 5 kV, the CL intensities of both the as-prepared $La(OH)_3$:0.05Eu^{3+} and La_2O_3:0.05Eu^{3+} samples increased with an increase of filament current from 35 to 55 μA and no saturation was observed up to 55 μA. Fig. 13(b) and (d) shows the increased CL intensities for both $La(OH)_3$:0.05Eu^{3+} and La_2O_3:0.05Eu^{3+} samples with increasing accelerating voltage from 1 to 5 kV under a fixed filament current of 55 μA. The reason behind the increased CL

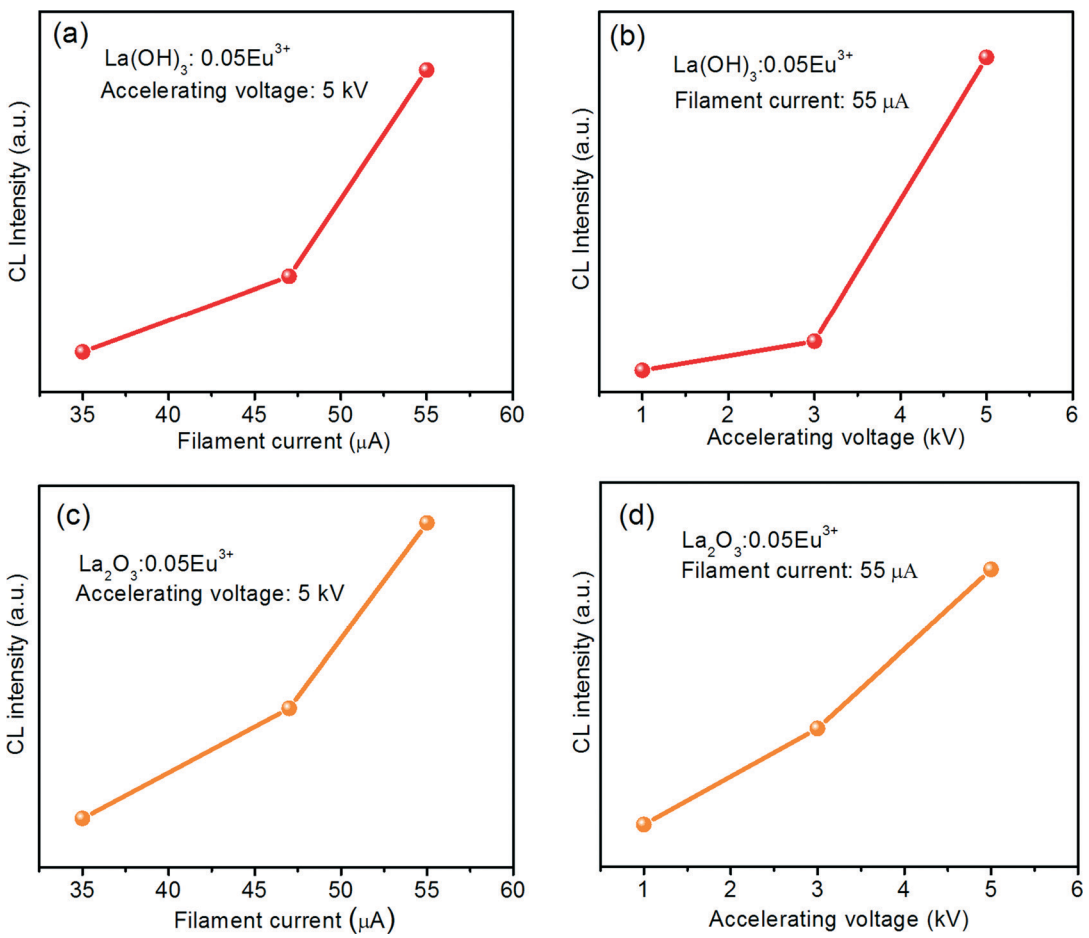

Fig. 13 Comparison of CL intensities as a function of (a and c) filament current for $La(OH)_3$:0.05Eu^{3+} and La_2O_3:0.05Eu^{3+} samples and (b and d) accelerating voltage for $La(OH)_3$:0.05Eu^{3+} and La_2O_3:0.05Eu^{3+} samples.

intensity for both samples is that the Eu^{3+} ions are excited through plasma produced by incident electrons. When the electron penetration depth becomes deeper, more plasma will be produced, thus producing more Eu^{3+} ions being excited. Hence, the CL intensity increased.[9,32] Thus, from the behavior of the increased CL intensity with increasing the filament current and accelerating voltage and also from the comparative study with the commercial Y_2O_3:Eu^{3+} phosphor, we are able to suggest that these $La(OH)_3$:0.05Eu^{3+} and La_2O_3:0.05Eu^{3+} phosphor samples are potential red phosphors in the development of FED systems.

Fig. 14 shows the Commission Internationale de L'Eclairage (CIE) chromaticity coordinates calculated from the PL and CL spectra of La_2O_3:0.05Eu^{3+} phosphors synthesized by the facile wet-chemical and solid-state reaction methods. The calculated CIE chromaticity coordinates from the PL emission of the La_2O_3:0.05Eu^{3+} phosphor with 3D flower-like nanorod bundles and solid-state reaction based La_2O_3:0.05Eu^{3+} phosphor were (0.647, 0.344) and (0.643, 0.356), respectively. Clearly, the La_2O_3:0.05Eu^{3+} 3D flower-like nanorod bundle phosphor has a higher red color purity compared to the solid-state reaction based La_2O_3:0.05Eu^{3+} phosphor. Hence, the obtained PL results suggest that the emission intensity and color purity of the La_2O_3:0.05Eu^{3+} nanorod bundle phosphor are better than those of the solid-state reaction based La_2O_3:0.05Eu^{3+} phosphor. Similarly, in order to compare the color richness in the CL spectra, the calculated CIE chromaticity coordinates of the La_2O_3:0.05Eu^{3+} 3D flower-like nanorod bundle phosphos were compared with those of the commercially available Y_2O_3:Eu^{3+} phosphor. The La_2O_3:0.05Eu^{3+} 3D flower-like nanorod bundle phosphor revealed much better chromaticity coordinates (0.651, 0.347) in the red region than the commercially available Y_2O_3:Eu^{3+} phosphor (0.621, 0.375), which supports the given explanation about the CL efficiency in the CL section.

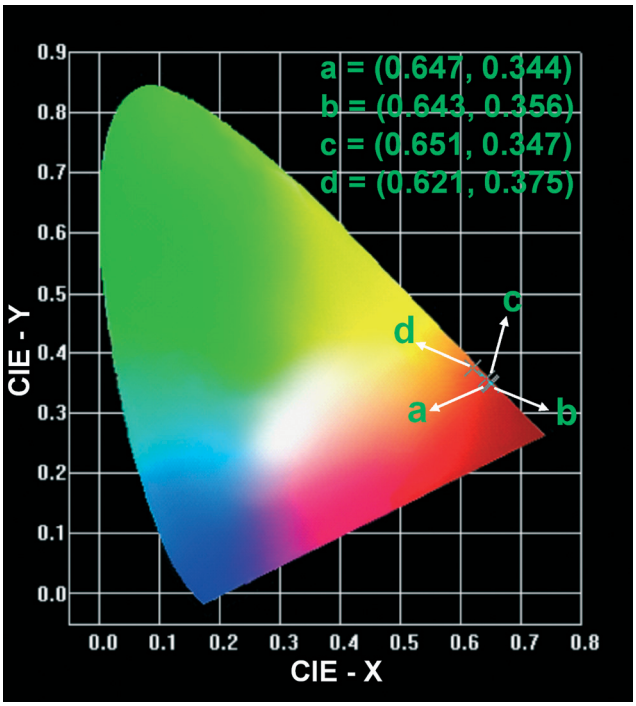

Fig. 14 CIE chromaticity coordinates: (a) La_2O_3:0.05Eu^{3+} nanorod bundle phosphor (0.647, 0.344) from PL, (b) solid-state reaction based La_2O_3:0.05Eu^{3+} phosphor (0.643, 0.356) from PL, (c) La_2O_3:0.05Eu^{3+} nanorod bundle phosphor (0.651, 0.347) from CL, and (d) commercial Y_2O_3:Eu^{3+} phosphor (0.621, 0.375) from CL.

Conclusions

In summary, self-assembled 3D flower-like nanorod bundles of $La(OH)_3$:0.05Eu^{3+} were successfully synthesized by a facile wet-chemical method. The XRD patterns exhibited a hexagonal structure, and the FTIR spectra confirmed the presence of OH^- group of $La(OH)_3$:0.05Eu^{3+} nanorod bundles. From SEM and TEM measurements, it is clear that the 3D flower-like morphology was formed by both crystal splitting and self-assembly process. The growth mechanism was discussed as a function of reaction time. After calcining the $La(OH)_3$:0.05Eu^{3+} samples, the XRD pattern confirmed the formation of the La_2O_3:Eu^{3+} phase. The effect of calcination on the morphology of La_2O_3:Eu^{3+} was also examined by SEM and TEM. The PL and CL studies were performed for the $La(OH)_3$:0.05Eu^{3+} and La_2O_3:Eu^{3+} samples. From the PL spectral properties, the synthesized La_2O_3:0.05Eu^{3+} nanorod bundle phosphor showed a higher asymmetric ratio value than the solid-state reaction based La_2O_3:0.05Eu^{3+} phosphor. Furthermore, in the CL study, the La_2O_3:0.05Eu^{3+} phosphor exhibited higher CL intensity, higher FWHM value, and at the same time much better CIE chromaticity coordinates than the commercially available Y_2O_3:Eu^{3+} phosphor. Finally, from the above analysis, we are able to suggest that the $La(OH)_3$:Eu^{3+} and La_2O_3:Eu^{3+} phosphors with self-assembled 3D flower-like nanorod bundles are promising materials for application in the development of novel optical systems such as FEDs, cathode ray tubes, plasma display panels, fluorescent lamps, *etc.*

Acknowledgements

This work was supported by a grant from the National Research Foundation of Korea (NRF) funded by the Korean government (MSIP) (No. 2014-069441).

References

1 G. S. R. Raju, E. Pavitra and J. S. Yu, *Dalton Trans.*, 2013, **42**, 11400–11410.
2 Z. Xu, C. Li, D. Yang, W. Wang, X. Kang, M. Shang and J. Lin, *Phys. Chem. Chem. Phys.*, 2010, **12**, 11315–11324.
3 A. K. Parchur, A. I. Prasad, A. A. Ansari, S. B. Rai and R. S. Ningthoujam, *Dalton Trans.*, 2012, **41**, 11032–11045.
4 A. K. Parchur, A. I. Prasad, S. B. Rai and R. S. Ningthoujam, *Dalton Trans.*, 2012, **41**, 13810–13814.
5 J. Yang, C. Li, Z. Quan, C. Zhang, P. Yang, Y. Li, C. Yu and J. Lin, *J. Phys. Chem. C*, 2008, **112**, 12777–12785.
6 N. Zhang, W. Bu, Y. Xu, D. Jiang and J. Shi, *J. Phys. Chem. C*, 2007, **111**, 5014–5019.
7 M. Runowski, T. Grzyb, A. Zep, P. Krzyczkowska, E. Gorecka, M. Giersig and S. Lis, *RSC Adv.*, 2014, **4**, 46305–46312.

8 N. Imanaka, *J. Ceram. Soc. Jpn.*, 2005, **113**, 387–393.
9 G. Li, C. Peng, C. Zhang, Z. Xu, M. Shang, D. Yang, X. Kang, W. Wang, C. Li, Z. Cheng and J. Lin, *Inorg. Chem.*, 2010, **49**, 10522–10535.
10 N. Hirosaki, R.-J. Xie, K. Inoue, T. Sekiguchi, B. Dierre and K. Tamura, *Appl. Phys. Lett.*, 2007, **91**, 061101.
11 B. C. Cheng, Z. Y. Ouyang, B. X. Tian, Y. H. Xiao and S. J. Lei, *Ceram. Int.*, 2013, **39**, 7379–7386.
12 Z.-L. Wang, H. Chan, H.-L. Li and J. Hao, *Appl. Phys. Lett.*, 2008, **93**, 141106.
13 M. Vaseem, A. Umar, S. H. Kim and Y.-B. Hahn, *J. Phys. Chem. C*, 2008, **112**, 5729–5735.
14 G. S. R. Raju, E. Pavitra and J. S. Yu, *Phys. Chem. Chem. Phys.*, 2014, **16**, 18124–18140.
15 G. Li, C. Li, Z. Xu, Z. Cheng and J. Lin, *CrystEngComm*, 2010, **12**, 4208–4216.
16 M. Aghazadeh, A. N. Golikand, M. Ghaemi and T. Yousefi, *J. Electrochem. Soc.*, 2011, **158**, E136–E141.
17 R. Zhao, L. Wang, Z.-F. Chai and W.-Q. Shi, *RSC Adv.*, 2014, **4**, 52209–52214.
18 Z. Zhuang, X. Xue and Z. Lin, *Phys. Chem. Chem. Phys.*, 2015, **17**, 4845–4848.
19 J. Tang and A. P. Alivisatos, *Nano Lett.*, 2006, **6**, 2701–2706.
20 A. T. Kelly, I. Rusakova, T. Ould-Ely, C. Hofmann, A. Lüttge and K. H. Whitmire, *Nano Lett.*, 2007, **7**, 2920–2925.
21 H. Zhang, D.-H. Ha, R. Hovden, L. F. Kourkoutis and R. D. Robinson, *Nano Lett.*, 2010, **11**, 188–197.
22 Z. Deng, D. Chen, F. Tang, X. Meng, J. Ren and L. Zhang, *J. Phys. Chem. C*, 2007, **111**, 5325–5330.
23 A. Neumann and D. Walter, *Thermochim. Acta*, 2006, **445**, 200–204.
24 S. Z. Markov, L. V. Ladeinova-Soboleva and A. M. Chernyshova, *Russ. Chem. Bull.*, 1961, **10**, 1805–1810.
25 X. Zhang, P. Yang, D. Wang, J. Xu, C. Li, S. Gai and J. Lin, *Cryst. Growth Des.*, 2011, **12**, 306–312.
26 E. Füglein and D. Walter, *J. Therm. Anal. Calorim.*, 2012, **110**, 199–202.
27 W. T. Carnall, P. R. Fields and K. Rajnak, *J. Chem. Phys.*, 1968, **49**, 4450–4455.
28 E. Pavitra and J. Su Yu, *Mater. Lett.*, 2013, **90**, 134–137.
29 I. L. V. Rosa, A. P. Maciel, E. Longo, E. R. Leite and J. A. Varela, *Mater. Res. Bull.*, 2006, **41**, 1791–1797.
30 G. S. R. Raju, E. Pavitra, G. Nagaraju and J. S. Yu, *Dalton Trans.*, 2015, **44**, 1790–1799.
31 G. Li, C. Li, C. Zhang, Z. Cheng, Z. Quan, C. Peng and J. Lin, *J. Mater. Chem.*, 2009, **19**, 8936–8943.
32 G. S. R. Raju, Y. H. Ko, E. Pavitra, J. S. Yu, J. Y. Park, H. C. Jung and B. K. Moon, *Cryst. Growth Des.*, 2011, **12**, 960–969.